RSC Advances

PAPER

View Article Online
View Journal | View Issue

Cite this: *RSC Adv.*, 2023, **13**, 8130

Effect of LLZO on the *in situ* polymerization of acrylate solid-state electrolytes on cathodes†

Kaiyun Xu,‡[a] Xiaoyu Zhou,‡[a] Menghan Ge,[a] Ziwen Qiu,[a] Ya Mao,[b] Hefeng Wang,[a] Yinping Qin,[a] Jingjing Zhou,*[a] Yang Liu *[acd] and Bingkun Guo *[a]

Received 9th December 2022
Accepted 27th February 2023

DOI: 10.1039/d2ra07861a

rsc.li/rsc-advances

The comprehensive performance of the state-of-the-art solid-state electrolytes (SSEs) cannot match the requirements of commercial applications, and constructing an organic–inorganic composite electrolyte *in situ* on a porous electrode is an effective coping strategy. However, there are few studies focused on the influence of inorganic ceramics on the polymerization of multi-organic components. In this study, it was found that the addition of $Li_{6.4}La_3Zr_{1.4}Ta_{0.6}O_{12}$ (LLZO) weakens the interaction between different polymers and makes organic and inorganic components contact directly in the solid electrolyte. These suppress the segregation of components in the *in situ* polymerized composite SSE, leading to a decrease in the polymer crystallization and improvement of electrolyte properties such as electrochemical stability window and mechanical properties. The composite solid-state electrolyte can be *in situ* constructed on different porous electrodes, which can establish close contact with active material particles, showing an ionic conductivity 4.4×10^{-5} S cm^{-1} at 25 °C, and afford the ternary cathode stability for 100 cycles.

1 Introduction

As efficient energy storage systems, commercial rechargeable lithium ion batteries (LIBs) based on liquid electrolytes have gained great interest in the past few decades.[1–3] However, some intrinsic characteristics such as inflammability and safety issues come from liquid electrolytes, which make LIBs hardly be further optimized to meet the requirements of portable electronics and large-scale stationary energy storage systems.[4,5] Compared with liquid electrolytes, SSEs can present better thermal, electrochemical and mechanical properties during the working processes of high-energy density positive materials.[6,7] Moreover, SSEs can suppress the growth of lithium dendrites and afford the lithium metal anode used in LIBs, which indicates taking SSEs instead of liquid electrolytes in batteries will be obviously advantageous in improving the energy density of energy storage devices.[8–11] Thus, SSEs have been a research hotspot in recent years for high-performance lithium-based batteries.[12–15]

Inorganic solid electrolytes such as oxides,[16,17] sulfides[18,19] and halides[20] have excellent ionic conductivity, good thermal stability and incombustible properties. However, the inorganic SSEs are unstable *versus* the Li metal surface and/or atmosphere, indicating that the extra surface treatments are necessary for the ceramic.[21–23] Moreover, the high rigidity of inorganic SSEs not only inhibits lithium dendrite growth but also leads to huge interface impedances and complex production technologies, which make inorganic SSEs difficult for large-scale application. In contrast, polymer solid electrolytes[24] represented by polyoxyethylene (PEO) can alleviate the above-mentioned interface problems to a certain extent due to its good flexibility, easy processing and weather resistance.[25–27] However, the application of polymer solid electrolytes in high-energy density solid lithium batteries is confronted with challenges such as low ionic conductivity at room temperature (RT) and polymer degradation at the interface because of polymer solid electrolytes' ion transport mechanism and a narrow electrochemical stability window.[28–30] In general, the SSE with high ionic conductivity and good interfacial compatibility is the key of all-solid-state battery research.[31–35]

In situ building a composite film can produce SSEs with significantly improved comprehensive performances and break through the dilemma of solid-state LMBs.[36–40] Tu *et al.*[35] demonstrated a simple *in situ* ultraviolet solidification method by polymerizing poly(ethylene glycol) diacrylate (PEGDA), which produces the intimate electrode/electrolyte interface and make the cells exhibit small interfacial impedance, reduced

---

[a] Materials Genome Institute, Shanghai University, 99 Shangda Road, Baoshan District, Shanghai, China. E-mail: zjajzjj@t.shu.edu.cn; liuyang81@shu.edu.cn; guobingkun@shu.edu.cn

[b] Shanghai Institute of Space Power Sources, Shanghai, 200245, China

[c] A Key Laboratory of Advanced Energy Materials Chemistry (Ministry of Education), Nankai University, Tianjin, 300071, China

[d] Key Laboratory of Optoelectronic Chemical Materials and Devices of Ministry of Education, Jianghan University, No. 8, Sanjiaohu Rd., Wuhan, Hubei, 430056, P. R. China

† Electronic supplementary information (ESI) available. See DOI: https://doi.org/10.1039/d2ra07861a

‡ These authors contributed equally.

polarization, and excellent cycling stability. Nan *et al.*[36] introduced an *in situ* thermal polymerized composite SSE on different cathodes to establish Li-ion conductive paths and to decrease the interfacial resistance of the cathode/electrolyte interface, and make the $LiCoO_2$ cathode present a long cycle life at a loading of 11.09 mg cm^{-2}. *In situ* produced organic–inorganic composite SSEs have also been investigated. Guo *et al.*[37] designed the composite electrolytes with $Li_{6.25}Ga_{0.25}La_3Zr_2O_{12}$ (Ga-LLZO) nanoparticles as fillers. The *in situ* polymerized composite electrolytes are electrochemically stable up to 6.5 V *vs.* Li^+/Li and could show an ionic conductivity of 8×10^{-4} S cm^{-1} at 30 °C. Cui *et al.*[38] prepared a highly conductive 3D composite *via in situ* polymerization of an acrylate monomer in a self-supported 3D porous Li-argyrodite skeleton. The 3D composite SSE exhibits an ionic conductivity of 4.6×10^{-4} S cm^{-1} and supports the $LiN_{i0.8}Mn_{0.1}Co_{0.1}O_2$ cathode exhibit a high coulombic efficiency exceeding 99% at RT with a high working cut-off voltage of 4.5 V *vs.* Li^+/Li at 0.1C.

However, most of these works focus on the interaction of single organic-inorganic or organic–organic components in SSEs, and there are few investigations on inorganic fillers' influence on the *in situ* polymerization of composite SSEs. In this work, the effects of inorganic components on the *in situ* construction of multicomponent SSEs on the electrode surface were investigated. It was found that the addition of inorganic ceramics changes the interaction mode between original organic components. The results indicate that the hydrogen bonding action in PA2-PEO is inhibited by adding various amounts of LLZO, which suppresses the SSE component segregation and improves the ionic conductivity and mechanical strength of SSE.

2 Methods

2.1 Preparation

The cathode materials ($LiFePO_4$ and $LiNi_{1/3}Co_{1/3}Mn_{1/3}O_2$) were obtained from QingTao Energy Development Co., Ltd., and auxiliary materials such as polyvinylidene fluoride (PVDF) and acetone black were purchased from Hefei Kejing Materials Technology CO., Ltd. Di(ethylene glycol) diacrylate (A2, 98%), 2-hydroxy-2-methyl-1-phenyl-1-propanone (HMPP, 97%) and other materials were bought from Alfa Asear and used without further purification. LiTFSI and PC/acetonitrile (1 : 1, v/v) were mixed in a mass ratio of 6 : 4, and then 30 wt% of PEO (MW 30,000) was added and stirred at 60 °C for 8 hours to get Solution A. Following this, 0.02 g HMPP (2-hydroxy-2-methyl-1-phenyl-1-propanone) and 3.0 g ETPTA (A2: diethylene glycol diallyl ether) were mixed and stirred overnight to obtain Solution B. Then, Solution C was obtained by mixing Solution A and Solution B in a molar ratio of ETPTA/Li+ of 1 : 1. Subsequently 400 μL Solution C with different contents of $Li_{6.4}La_3Zr_{1.4}Ta_{0.6}O_{12}$(LLZO) was dripped onto a Φ10 mm cathode, vacuumed for 2 min, and exposed to UV light (365 nm, 35 W) at a distance of 5 mm for 1 h. Finally, the electrodes were placed on a heating table at 60 °C to fully evaporate the solvent, yielding the *in situ* formed solid electrolyte films on cathodes. The loading of the $LiFePO_4$ cathode is ∼2.8 mg cm^{-2} and that of the $LiNi_{1/3}Co_{1/3}Mn_{1/3}O_2$(NCM111) cathode is ∼2.3 mg cm^{-2}.

2.2 Characterization

The SSE films were vacuum-dried before measurements. Fourier-transform infrared (FTIR) spectra were recorded using a Nicolet 6700 with a resolution of 0.02 cm^{-1}. Scanning electron microscope (SEM) tests were implemented using a ZEISS, MERLIN Compact. The X-ray diffraction (XRD) patterns were acquired using a D8, Bruker, with Cu K radiation. Differential scanning calorimetry (DSC) measurements were carried out using a DSC214, NETZSCH at a heating rate of 10 °C min^{-1} in a N_2 atmosphere. Dynamic thermomechanical analysis (DMA) was performed using a DMA Q800, Waters Corporation.

2.3 Electrochemical testing

The ionic conductivity, electrochemical impedance and linear sweep voltammetry (LSV) measurements were performed using a Solartron 1470E. The cyclic and rate performances were tested using a LANHE CT2001A.

3 Results and discussion

In this work, LLZO was used to study the influence of inorganic fillers in the polymerization of monomers on a porous electrode. The differential scanning calorimetry (DSC) test was conducted to investigate the interaction-induced differences in the thermodynamic properties of the samples. While the melting temperature (T_m) is lifted slightly, the glass transition temperatures (T_g) of composite electrolytes are generally reduced by the addition of LLZO (Fig. 1a). With 10 wt% LLZO added, the sample presented a really low T_g of −53 °C and a barely visible melting enthalpy region. This suggests the film PA2-PEO-10% LLZO may present a higher disorder degree than that of other samples at RT.

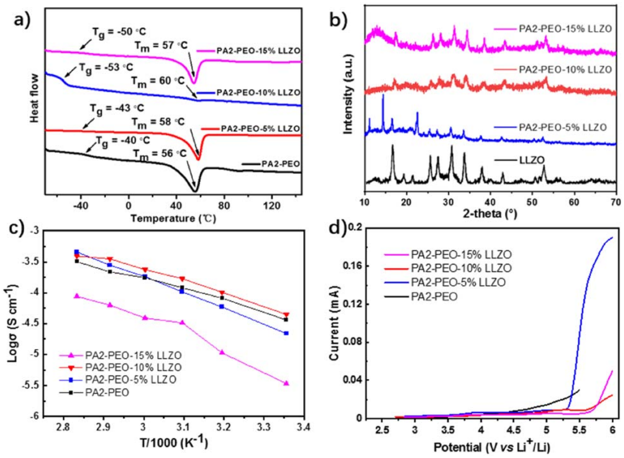

Fig. 1 DSC (a), XRD (b), Arrhenius plots of conductivity (c) and LSV (d) curves of films with different contents of LLZO at 25 °C. Scan rate: 0.5 mV s^{-1}.

X-ray diffraction (XRD) was used to investigate the degree of crystallinity of the samples (Fig. 1b). It is clear that the peaks of LLZO in the electrolyte films are sharper with the addition of more LLZO, and the peaks of PEO at ~11, 14, and 22.5° are visible in the two samples with 5 wt% and 15 wt% LLZO added; the peaks of PEO are sharp in the sample with 5 wt% LLZO added and broad with 15 wt% LLZO added, as less addition of LLZO can make the segregation of PEO. However, it is hard to detect the peaks of PEO in 10 wt% LLZO-added sample.[41] These can be explained as that with 10 wt% LLZO added, and LLZO is interacted with both of PA2 and PEO, leading to the peaks of PEO that cannot be obviously detected and resulting in the lowest crystallinity of PA2-PEO-10% LLZO among all the samples, which is consistent with the results obtained by DSC.

A variable temperature AC impedance test shows a bell-curve-like relationship between the conductivities and LLZO contents of SSEs (Fig. 1c). When 10 wt% LLZO is added, the film presents the highest conductivity up to 4.4×10^{-5} S cm^{-1} at RT. The conductivity of PA2-PEO-5% LLZO is lower at a low temperature (<60 °C) and higher at a high temperature than that of PA2-PEO. In addition, the conductivity of PA2-PEO-15% LLZO is lower than that of other films at both low and high temperatures. Considering the disintegrate effect of LLZO on the interaction of PA2 & PEO, it should be understood that PEO in the 5 wt% LLZO-added film presents a higher crystallinity degree at low temperatures and a lower crystallinity degree at high temperatures, which leads to the different conductivity of PA2-PEO-5% LLZO at different temperatures. In addition, the agglomeration of LLZO particles makes the 15 wt% LLZO-added sample shows a lower conductivity at different temperatures. The addition of LLZO also greatly improves the electrochemical stability of PA2-PEO (Fig. 1d). While 10 wt% LLZO is added, the sample presents a high electrochemical window, up to 5.5 V *vs.* Li^+/Li and the lowest oxidation current at a higher potential (~6 V *vs.* Li^+/Li) among the films.

Fourier transform infrared (FTIR) spectroscopy was performed to confirm the interaction between PA2, PEO and LLZO. The molecular structure of di(ethylene glycol) diacrylate (A2) is shown in Fig. 2, and PA2 was produced as the work we reported. As shown in Fig. 2, the peak at ~1050 cm^{-1} in PEO, which should be related to the ether oxygen group, is blue-shifted in PA2-PEO but stay in step with that in PA2-PEO-10% LLZO. The peak at ~1730 cm^{-1} in PA2 is slightly shifted in PA2-PEO, and is hard to be detected in PA2-PEO-10% LLZO. As shown in Fig. 2, the peak at ~1050 cm^{-1} in PEO, which points to the ether oxygen group, is slightly blue-shifted in PEO-LLZO and obviously blue-shifted in PA2-PEO. The former should be related to the interaction between PEO & LLZO and the latter should be related to PA2 & PEO. Considering this peak is gradually blue-shifted in the samples, while the content of LLZO is increased (Fig. S1†), and a similar peak of at ~1730 cm^{-1} in PA2-PEO cannot be detected in PA2-PEO-LLZO samples, and the results indicate the addition of LLZO inhibits the interaction between PA2 & PEO, and presents an interaction between PEO & LLZO. Moreover, a similar trend is detected in the PA2-contained samples at a peak of ~1070 cm^{-1}, which is related to the ether oxygen group of PA2, meaning the interaction between PA2 & LLZO (Fig. S1†). Considering the signature peak at ~1730 cm^{-1} of PA2-PEO cannot be detected in the samples with LLZO added (Fig. 2), these results further confirm that the addition of LLZO inhibits the interaction between PA2 & PEO, and presents the interaction between PEO & LLZO and PA2 & LLZO. The forceful interactions between organic and inorganic components may influence the structure and physical and chemical properties of the composite solid-state electrolyte. The slight shifting at ~1175 cm^{-1} also means the directly interaction of LLZO and PEO. The peaks at ~650 cm^{-1} that could be assigned to C–H are detected in both PA2-PEO and PA2-PEO-LLZO. This should be attributed to the interaction of PA2 and PEO, and the interaction also exists in both of PA2-PEO and PA2-PEO-10% LLZO, which can explain the variability of peaks detected by XRD.

Dynamic thermomechanical analysis (DMA) measurement was carried to detail the stress–strain relationships of PA2-PEO-10% LLZO and PA2-PEO film, as shown in Fig. S2.† PA2-PEO-10% LLZO and PA2-PEO present completely different states, while PA2-PEO-10% LLZO shows direct brittle fracture at the limit of yielding and PA2-PEO is in a viscoelastic state. The maximum stress of PA2-PEO is 0.5 MPa. By contrast, the maximum stress of PA2-PEO-10% LLZO is 3.5 MPa, almost six times stronger than that of the pure-polymer-electrolyte. The higher mechanical strength should possess PA2-PEO-10% LLZO with better ability to deal with the growth of lithium dendrite and volume deformation of Li in cycling.

Scanning electron microscopy (SEM) reveals the morphologies of composite electrolytes. As shown in Fig. 3a–c, PA2-PEO-10% LLZO has a relatively uniform surface compared with 5 or 15 wt% LLZO-added films. The similar phenomena are also

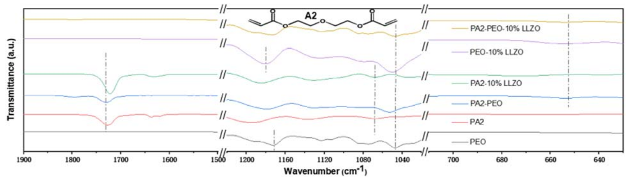

Fig. 2 FTIR spectra of PEO, PA2, PA2-PEO, PA2-10% LLZO, PEO-10% LLZO and PA2-PEO-10% LLZO films. Inset is the molecular structure of A2.

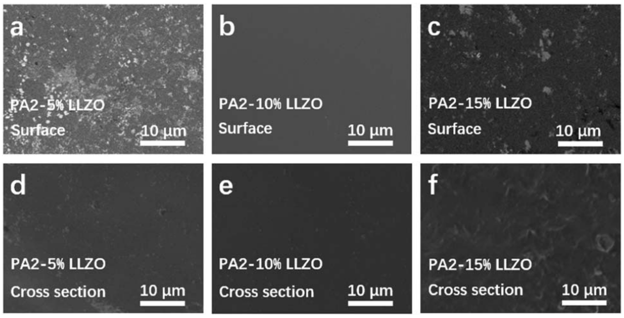

Fig. 3 Surface and cross-section morphology of different films.

detected in the cross section SEM images of the samples. Components agglomerate inside 5 or 15 wt% LLZO-added films, and no distinct bright bulge is clearly visible in Fig. 3e. The results mean that the distribution of LLZO is uniform and no segregation of PA2 or PEO can be detected in PA2-PEO-10% LLZO, which should be attributed to the homogeneity of the composite material.

Then, the composite electrolytes were *in situ* polymerized on $LiFePO_4$ cathodes, and electrochemical impedance spectroscopy (EIS) measurement was taken to investigate the interface impedance in electrode–electrolyte complexes. As shown in Fig. 4a, the resistance of interface layer (R_{sei}, corresponding to the first semicircle) and charge movement (R_{ct}, corresponding to the second semicircle) of LLZO-added sample are much smaller than that of PA2-PEO only. These results indicate that the electrochemical kinetic at the electrode/electrolyte interface is improved by the addition of inorganic ceramic fillers. The stabilities of solid electrolytes *versus* lithium metal at RT are compared, as shown in Fig. 4b, using a Li/SSE/Li symmetrical cell. Both the SSEs maintain the relatively stable polarization potentials in 100 hours, and the compositing of LLZO reduces the polarization potential remarkably from ~0.3 V to ~0.2 V. These will be in favor of reducing the battery internal resistance. The SEM images concur with the above-mentioned results. The Li anode cycled with PA2-PEO presents a chapped surface and the Li anode in the PA2-PEO-10% LLZO battery presents a much smoother surface (Fig. 4c and d). These results indicate that the LLZO-reinforced SSE dramatically suppresses the growth of Li dendrites, which enhances the stabilities of SSEs on the Li anode and reduces the polarization potential at the SSE/Li interface.

Solid-state LMBs were assembled and investigated at RT to evaluate the electrochemical performance of PA2-PEO-10% LLZO on different cathodes. The $LiFePO_4$-based battery displays a high reversible capacity of 142 mA h g^{-1} with a good capacity retention of ~87.3% in 50 cycles at RT (Fig. 5a). Fig. S3† shows the flat charge–discharge curves and very small polarization voltage, indicating the low interfacial impedance of the all-solid-state battery. Furthermore, the electrolyte PA2-PEO-10% LLZO was tried on the $LiNi_{1/3}Co_{1/3}Mn_{1/3}O_2$(NCM111) cathode. As shown in Fig. 5b, the NCM111/PA2-PEO-10% LLZO/Li battery presents a reversible capacity of ~139 mA h g^{-1} at 0.1C, 60 °C and retains ~79.5% in 100 cycles between 2.5 and 4.2 V *vs.* Li^+/Li. While cycled between 2.5 and 4.4 V *vs.* Li^+/Li, the NCM111/PA2-PEO-10% LLZO/Li cell shows an initial discharge capacity of 162 mA h g^{-1} at 0.1C, 60 °C, and remains 124 mA h g^{-1} in 50 cycles (Fig. S4†). These results indicate that PA2-PEO-10% LLZO can afford excellent interfacial compatibility in cycling on the cathode with a high operating potential. The battery also achieves a good rate performance with capacities of 136, 111.1, 92.7, and 75.3 mA h g^{-1} at current rates of 0.1, 0.2, 0.3 and 0.4C respectively (Fig. S5†). When the current rate return to 0.1C, the discharging capacity is almost restored. While operated at a higher rate, the NCM111/PA2-PEO-10% LLZO/Li cell shows an initial discharge capacity of ~80 mA h g^{-1} at 1C, 60 °C and fades quickly in 40 cycles with a reversible capacity of ~50 mA h g^{-1} (Fig. S6†). These evidences suggest the strategy of evolving SSE interfacial compatibility, and the electrochemical stability shown in this work is promising for the improvement of high–energy density solid-state lithium batteries. Moreover, to investigate the electrochemical properties of PA2-PEO-5% LLZO and PA2-PEO-15% LLZO, the corresponding cells with $LiFePO_4$ and NCM111 cathodes were assembled. Both of $LiFePO_4$/PA2-PEO-5% LLZO/Li and $LiFePO_4$/PA2-PEO-15% LLZO/Li cells present the initial discharge capacities of ~160 mA h g^{-1} and fade quickly in the following cycles at 0.1C, 25 °C (Fig. S7a and b†). Then, the NCM111/PA2-PEO-5% LLZO/Li and NCM111/PA2-PEO-15% LLZO/Li cells were tested at 0.1C, 60 °C. These cells present an initial discharge capacity of ~120 mA h g^{-1} and unstable coulombic efficiency in 20 cycles (Fig. S7c and d†). The above-mentioned results should be related to the contents of LLZO, which affect the segregation of the solid electrolyte components.

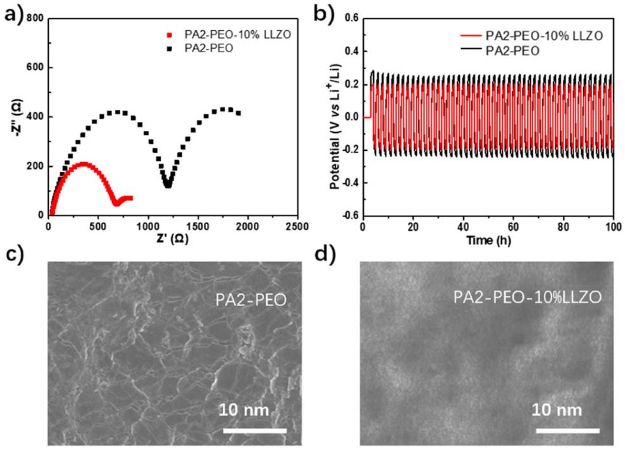

Fig. 4 EIS (a) of $LiFePO_4$/PA2-PEO-10% LLZO/Li batteries, galvanostatic cycling of the symmetrical cell (b) 0.13 mA cm^{-2} at 25 °C, and the SEM images (c and d) of Li metal anodes cycled with different SSEs.

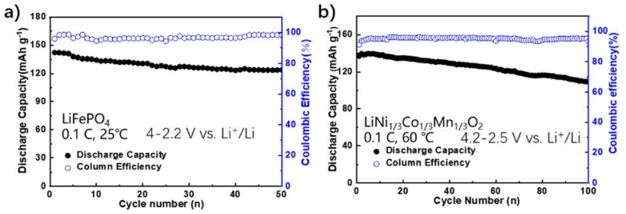

Fig. 5 Cyclic performance of $LiFePO_4$/PA2-PEO-10% LLZO/Li cells at 0.1C, 25 °C, and NCM111/PA2-PEO-10% LLZO/Li cells at 60 °C.

4 Conclusion

In summary, a LLZO-reinforced SSE has been successfully *in situ* fabricated on porous cathodes. The addition of ceramic fillers inhibits the component segregation in the SSE by weakening the interaction between different polymers, which makes organic and inorganic components contact directly in the solid electrolyte. The SSE also exhibits good mechanical strength due to the strong interaction between inorganic ceramics and polymers. The addition of LLZO increases the conductivity of SSE to 4.4×10^{-5} S cm^{-1} at RT and makes the membrane show excellent interfacial compatibilities on both the Li metal anode and porous cathodes. Benefiting from these, the polarization of the Li/SPE/Li symmetrical cell is reduced by ~30%, the solid $LiFePO_4$/PA2-PEO-10% LLZO/Li cells display a good cycling stability with a capacity retention of ~87.3% at RT, and the NCM111/PA2-PEO-10% LLZO/Li battery presents excellent performances with a discharging capacity of 139 mA h g^{-1} and a retention of ~79.5% in 100 cycles at 60 °C. These results provide a new recipe for high-voltage solid-state LMBs, and a deeper understanding of design strategy evolution for other high-performance SSEs in all-solid-state lithium batteries.

Conflicts of interest

There are no conflicts to declare.

Acknowledgements

This work supported by the National Natural Science Foundation of China (Grant No. 22075172), the Opening Project of Key Laboratory of Optoelectronic Chemical Materials and Devices of Ministry of Education, Jianghan University(JDGD-202221), the Science and Technology Commission of Shanghai Municipality (20511107800) and 111 project (D16002).

References

1 X. B. Cheng, R. Zhang, C. Z. Zhao and Q. Zhang, *Chem. Rev.*, 2017, **117**, 10403–10473.
2 D. Lin, Y. Liu and Y. Cui, *Nat. Nanotechnol.*, 2017, **12**, 194–206.
3 C. Sun, J. Liu, Y. Gong, D. P. Wilkinson and J. Zhang, *Nano Energy*, 2017, **33**, 363–386.
4 F. Cheng, J. Liang, Z. Tao and J. Chen, *Adv. Mater.*, 2011, **23**, 1695–1715.
5 H. Wang, L. Sheng, G. Yasin, L. Wang, H. Xu and X. He, *Energy Storage Mater.*, 2020, **33**, 188–215.
6 D. Xu, J. Su, J. Jin, C. Sun, Y. Ruan, C. Chen and Z. Wen, *Adv. Energy Mater.*, 2019, **9**, 1900611.
7 J. Liu, Z. Bao, Y. Cui, E. J. Dufek, J. B. Goodenough, P. Khalifah, Q. Li, B. Y. Liaw, P. Liu, A. Manthiram, Y. S. Meng, V. R. Subramanian, M. F. Toney, V. V. Viswanathan, M. S. Whittingham, J. Xiao, W. Xu, J. Yang, X.-Q. Yang and J.-G. Zhang, *Nat. Energy*, 2019, **4**, 180–186.
8 G. Li and C. W. Monroe, *Phys. Chem. Chem. Phys.*, 2019, **21**, 20354–20359.
9 H. Liu, X.-B. Cheng, J.-Q. Huang, H. Yuan, Y. Lu, C. Yan, G.-L. Zhu, R. Xu, C.-Z. Zhao, L.-P. Hou, C. He, S. Kaskel and Q. Zhang, *ACS Energy Lett.*, 2020, **5**, 833–843.
10 X. X. Zeng, Y. X. Yin, N. W. Li, W. C. Du, Y. G. Guo and L. J. Wan, *J. Am. Chem. Soc.*, 2016, **138**, 15825–15828.
11 N. W. Li, Y. Shi, Y. X. Yin, X. X. Zeng, J. Y. Li, C. J. Li, L. J. Wan, R. Wen and Y. G. Guo, *Angew. Chem., Int. Ed. Engl.*, 2018, **57**, 1505–1509.
12 D. Lin, W. Liu, Y. Liu, H. R. Lee, P. C. Hsu, K. Liu and Y. Cui, *Nano Lett.*, 2016, **16**, 459–465.
13 K. Pan, L. Zhang, W. Qian, X. Wu, K. Dong, H. Zhang and S. Zhang, *Adv. Mater.*, 2020, **32**, e2000399.
14 N. Wu, P. H. Chien, Y. Li, A. Dolocan, H. Xu, B. Xu, N. S. Grundish, H. Jin, Y. Y. Hu and J. B. Goodenough, *J. Am. Chem. Soc.*, 2020, **142**, 2497–2505.
15 M. Ge, X. Zhou, Y. Qin, Y. Liu, J. Zhou, X. Wang and B. Guo, *Chin. Chem. Lett.*, 2022, **33**, 3894–3898.
16 M. Hema, P. Tamilselvi and G. Hirankumar, *Ionics*, 2016, **23**, 2707–2714.
17 X. Zuo, J. Wu, X. Ma, X. Deng, J. Cai, Q. Chen, J. Liu and J. Nan, *J. Power Sources*, 2018, **407**, 44–52.
18 A. H. Ryoichi Komiya, H. Morimoto, M. Tatsumisago and T. Minami, *Solid State Ionics*, 2001, **140**, 83–87.
19 S. Ujiie, T. Inagaki, A. Hayashi and M. Tatsumisago, *Solid State Ionics*, 2014, **263**, 57–61.
20 X. Li, J. Liang, X. Yang, K. R. Adair, C. Wang, F. Zhao and X. Sun, *Energy Environ. Sci.*, 2020, **13**, 1429–1461.
21 X. Chen, W. He, L.-X. Ding, S. Wang and H. Wang, *Energy Environ. Sci.*, 2019, **12**, 938–944.
22 Q. Guo, Y. Han, H. Wang, S. Xiong, W. Sun, C. Zheng and K. Xie, *Electrochim. Acta*, 2019, **296**, 693–700.
23 B. Chen, Z. Huang, X. Chen, Y. Zhao, Q. Xu, P. Long, S. Chen and X. Xu, *Electrochim. Acta*, 2016, **210**, 905–914.
24 Z. Lv, Y. Tang, S. Dong, Q. Zhou and G. Cui, *Chem. Eng. J.*, 2022, **430**, 132659.
25 J. Chai, Z. Liu, J. Zhang, J. Sun, Z. Tian, Y. Ji, K. Tang, X. Zhou and G. Cui, *ACS Appl. Mater. Interfaces*, 2017, **9**, 17897–17905.
26 Q. Liu, Z. Geng, C. Han, Y. Fu, S. Li, Y.-b. He, F. Kang and B. Li, *J. Power Sources*, 2018, **389**, 120–134.
27 J. Zhang, J. Zhao, L. Yue, Q. Wang, J. Chai, Z. Liu, X. Zhou, H. Li, Y. Guo, G. Cui and L. Chen, *Adv. Energy Mater.*, 2015, **5**, 1501082.
28 X. Wang, R. Kerr, F. Chen, N. Goujon, J. M. Pringle, D. Mecerreyes, M. Forsyth and P. C. Howlett, *Adv. Mater.*, 2020, **32**, e1905219.
29 W. Zhang, S. Zhang, L. Fan, L. Gao, X. Kong, S. Li, J. Li, X. Hong and Y. Lu, *ACS Energy Lett.*, 2019, **4**, 644–650.
30 Q. Zhou, J. Ma, S. Dong, X. Li and G. Cui, *Adv. Mater.*, 2019, **31**, 1902029.
31 L. Chen, Y. Li, S.-P. Li, L.-Z. Fan, C.-W. Nan and J. B. Goodenough, *Nano Energy*, 2018, **46**, 176–184.
32 Z. Wei, Z. Zhang, S. Chen, Z. Wang, X. Yao, Y. Deng and X. Xu, *Energy Storage Mater.*, 2019, **22**, 337–345.
33 Q. Liu, B. Cai, S. Li, Q. Yu, F. Lv, F. Kang, Q. Wang and B. Li, *J. Mater. Chem. A*, 2020, **8**, 7197–7204.
34 M. Wu, D. Liu, D. Qu, J. Lei, X. Zhang, H. Chen and H. Tang, *J. Colloid Interface Sci.*, 2022, **615**, 627–635.
35 S. Z. Zhang, X. H. Xia, D. Xie, R. C. Xu, Y. J. Xu, Y. Xia, J. B. Wu, Z. J. Yao, X. L. Wang and J. P. Tu, *J. Power Sources*, 2019, **409**, 31–37.
36 C. Xin, X. Zhang, C. Xue, S. Wang, L. Li and C.-W. Nan, *Solid State Ionics*, 2020, 345.

37 Z. Li, H.-X. Xie, X.-Y. Zhang and X. Guo, *J. Mater. Chem. A*, 2020, **8**, 3892–3900.

38 Y. Wang, J. Ju, S. Dong, Y. Yan, F. Jiang, L. Cui, Q. Wang, X. Han and G. Cui, *Adv. Funct. Mater.*, 2021, **31**, 2101523.

39 Q. Zhou, S. Dong, Z. Lv, G. Xu, L. Huang, Q. Wang, Z. Cui and G. Cui, *Adv. Energy Mater.*, 2020, **10**, 1903441.

40 Z. Lv, Q. Zhou, S. Zhang, S. Dong, Q. Wang, L. Huang, K. Chen and G. Cui, *Energy Storage Mater.*, 2021, **37**, 215–223.

41 W. Wang, Z. Qiu, Q. Wang, X. Zhou, Y. Liu, J. Zhou, B. Guo and R. Soc, *Open Sci.*, 2020, **7**, 200598.